REGULAR ARTICLE

Construction of metal oxide decorated g-C$_3$N$_4$ materials with enhanced photocatalytic performance under visible light irradiation

T VINODKUMAR[a], P SUBRAMANYAM[a], K V ASHOK KUMAR[a], BENJARAM M REDDY[b] and CH SUBRAHMANYAM[a,*]

[a]Department of Chemistry, Indian Institute of Technology, Hyderabad 502 285, India
[b]Inorganic and Physical Chemistry Division, CSIR-Indian Institute of Chemical Technology, Uppal Road, Hyderabad 500 007, India
E-mail: csubbu@iith.ac.in

Abstract. Herein we report the synthesis and photocatalytic evaluation of heterostructure WO$_3$/g-C$_3$N$_4$ (WMCN) and CeO$_2$/g-C$_3$N$_4$ (CMCN) materials for RhB degradation and photoelectrochemical studies. These materials were synthesized by varying the dosages of WO$_3$ and CeO$_2$ on g-C$_3$N$_4$ individually and were characterized with state-of-the-art techniques like XRD, BET surface area, FT-IR, UV–Vis DRS, TGA, SEM, TEM and XPS. A collection of combined structural and morphological studies manifested the formation of bare g-C$_3$N$_4$, WO$_3$, CeO$_2$, WO$_3$/g-C$_3$N$_4$ and CeO$_2$/g-C$_3$N$_4$ materials. From the degradation results, we found that the material with 10 wt% WO$_3$ and 15 wt% CeO$_2$ content on g-C$_3$N$_4$ showed the highest visible light activity. The first order rate constant for the photodegradation performance of WMCN10 and CMCN15 is found to be 5.5 and 2.5 times, respectively, greater than that of g-C$_3$N$_4$. Photoelectrochemical studies were also carried out on the above materials. Interestingly, the photocurrent density of WMCN10 photoanode achieved 1.45 mA cm^{-2} at 1.23 V (vs.) RHE and this is much larger than all the prepared materials. This enhanced photoactivity of WMCN10 is mainly due to the cooperative synergy of WO$_3$ with g-C$_3$N$_4$, which enhanced the visible light absorption and suppresses the electron–hole recombination.

Keywords. g-C$_3$N$_4$; rhodamine B; photocatalysis; heterojunction.

1. Introduction

To alleviate the global energy and environmental issues, the development of renewable technologies has become increasingly inevitable and imperative to accomplish a potential sustainable-energy society. Among the numerous available renewable sources, interestingly, semiconductor photocatalysis has been receiving much attention because it represents a simple way to exploit the solar energy which significantly meets the requirements for the present issues on energy and environment.[1–3] In photocatalysis, the activity of the material depends mainly on light absorption capacity, separation, and transportation of photogenerated electrons and holes. Most of the materials fail to meet these conditions. Therefore, the design and development of effective photocatalytic materials have been a demanding task for the last few years.

In literature, many photoactive materials such as TiO$_2$, BiVO$_4$, Ag$_3$PO$_4$, ZnO, etc., were discussed in detail. However, their activity is limited to a certain extent only. Consequently, researchers have been looking for alternative photocatalysts. Recently, among the various kinds of active materials, polymeric g-C$_3$N$_4$ materials seize the attention due to their visible light response, easy synthesis, good stability, tunable electronic structure and a band gap around 2.7 eV. Most importantly, more negative conduction band edge for

g-C_3N_4 (-1.13 eV) provides the possibility to get access to overall water splitting or lower bias potential input. Recent citations on the g-C_3N_4 materials have witnessed their promising applications in various fields such as carbon dioxide reduction, purification of contaminated water, energy conversion, etc. Nonetheless, it suffers from low carrier mobility, and fast electron–hole recombination, which is a bottleneck that curbs the practical applications of g-C_3N_4.[4–8]

To prevail these impediments, some significant efforts have been attempted to increase the photocatalytic efficiency of g-C_3N_4 such as doping with metals or non-metals or formation of heterojunction with other semiconductor materials. In these, the formation of heterojunction materials has been considered as a potential way to enhance its performance. Primarily many composites including, metal oxide/g-C_3N_4, noble metal/g-C_3N_4, metal sulfide/g-C_3N_4, etc., are reported for H_2 production, pollutant degradation, etc., and has led to exciting and attractive developments. Therefore, for effective utilization of solar energy, fabricating g-C_3N_4 with other semiconductor materials is strongly needed.[9–12] Tungsten oxide (WO_3) possess excellent visible light activity due to its band gap of approximately 2.5–2.8 eV and its high chemical stability, environmental friendliness, natural abundance, etc.[13,14] On the other hand, cerium oxide (CeO_2) is also an important material in numerous applications like antioxidants in biological systems, production of green fuels, and an indispensable component of automotive and industrial catalysts, etc.[15–17] It can reserve and release oxygen when treated alternatively under oxidizing and reducing atmospheres. This oxygen buffer feature renders it as a fascinating candidate for redox catalysis and its resistance to chemical and photocorrosion, and strong light absorption in the UV region.[18–20] Based on this, both WO_3 and CeO_2 appear to be appealing candidates to construct the heterojunction with g-C_3N_4 individually. Furthermore, both the materials have more positive conduction and valence band edges than those of g-C_3N_4. Therefore, in the present study, we focused on the advancement of g-C_3N_4 materials by fabricating it with the WO_3 and CeO_2 separately by varying the amounts of WO_3 and CeO_2. The prepared materials were characterized using various state-of-the-art techniques like X-ray diffraction (XRD), Fourier transform infrared (FT-IR), Brunauer Emmett-Teller (BET) surface area, thermogravimetric analysis (TGA), scanning electron microscopy (SEM), transmission electron microscopy (TEM), UV-Visible diffuse reflectance spectroscopy (UV–Vis DRS), and X-ray photoelectron spectroscopy (XPS). Finally, the synthesized materials were tested for RhB degradation and photoelectrochemical (PEC) reactions.

2. Experimental

2.1 Materials

All chemicals used in this experiment were of the analytical grade without further purification.

2.1a Synthesis of g-C_3N_4: To synthesize g-C_3N_4, the desired amount of melamine powder was taken in an alumina crucible, which is covered and then heated in a muffle furnace at 550 °C for 4 h. After cooling to room temperature, the yellow powder (g-C_3N_4) was ground and collected for successive use.

2.1b Synthesis of WO_3: In the present study, WO_3 was prepared by dissolving $Na_2WO_4 \cdot 2H_2O$ (0.50 g) and NaCl (0.05 g) in 50 mL distilled water and its pH was adjusted to 2 using 10% HCl and stirred for 30 min. The resulting solution was transferred into 100 mL Teflon-lined autoclave and heated at 180 °C for 24 h. The formed material was filtered and washed with distilled water and ethanol. Finally, the obtained product was oven dried at 60 °C overnight and calcined at 450 °C for 4 h to get WO_3 samples.[21]

2.1c Synthesis of CeO_2: The required amount of Ce $(NO_3)_3 \cdot 6H_2O$ was dissolved in distilled water. To this 6 M NaOH solution was added dropwise to get the milky slurry and which was stirred for 30 min at room temperature. Subsequently, the solution was transferred into a 100 mL Teflon-lined autoclave and heated at 100 °C for 24 h. After cooling to room temperature, the solution was filtered and, washed with distilled water and ethanol several times, and dried at 80 °C overnight and finally calcined at 500 °C for 5 h.[22] The material is represented with C.

2.1d Synthesis of WO_3/g-C_3N_4 (WMCN) and CeO_2/g-C_3N_4 (CMCN) composites: In a typical synthesis of WO_3/g-C_3N_4[23] photocatalysts, various amounts of WO_3 with an appropriate amount of g-C_3N_4 were added into a mortar and then ground for 30 min using a pestle. The resultant powder was transferred into a crucible, which was covered and then heated in a muffle furnace at 450 °C for 4 h. The final WMCN photocatalysts with various WO_3 contents (5, 10 and 15 wt%) were obtained. The obtained materials were named as WMCN5, WMCN10, and WMCN15. A similar method was used to prepare ceria decorated g-C_3N_4 by varying the amounts of CeO_2 (5, 10, 15, and 20 wt%).[24] The obtained materials were designated as CMCN5, CMCN10, CMCN15, and CMCN20 respectively.

2.2 Materials characterization

The XRD data was acquired in the 2θ range of 12°–80° using a PANalytical X'pert Pro Powder X-Ray diffractometer with Cu-Kα radiation with wavelength λ = 1.54 Å and Ni is used as a filter. The applied current and accelerating voltage are maintained at 30 mA and 40 kV respectively during the measurement. The BET surface area measurements were

performed using a Micromeritics ASAP 2020 instrument. Prior to analysis, the samples were oven dried at 393 K for 12 h and flushed with Argon gas for 2 h. The BET surface area was measured using nitrogen adsorption–desorption isotherms at liquid nitrogen temperature. A Fourier transform infrared (FT-IR) spectrum of samples was recorded using a Bruker alpha spectrometer at room temperature. The optical properties of prepared samples were characterized using UV-Visible diffuse reflectance spectrophotometer (Shimadzu-3600) with $BaSO_4$ as a standard reference. Thermogravimetric analysis (TGA) was carried out using a Thermal Analyzer (SDT-Q600) from 300 to 1173K in an air flow of 100 mL/min at a heating rate of 10 °C/min. The morphology of prepared samples was investigated by FE-SEM (Gemini Supra 40 ZEISS) at 10 kV accelerating voltage. TEM studies were performed using a JEM-2100 (JEOL) instrument equipped with a slow-scan CCD camera at an accelerating voltage of 200 kV. The XPS measurements were performed using a Shimadzu (ESCA 3400) spectrometer by using Al K α (1486.7 eV) radiation as the excitation source. The charging effects of the catalyst samples were corrected using the binding energy of adventitious carbon (C 1s) at 284.6 eV as the internal reference. The XPS analysis was done at ambient temperature and pressures usually in the order of less than 10^{-8} Pa.

2.3 *Photocatalytic and photoelectrochemical studies*

Photocatalytic activities of synthesized catalysts are tested in a specially designed reactor using a 250 W halogen lamp. In a typical run, the 0.05 g catalyst was added to 50 mL of 5 mg L^{-1} RhB solution in a round-bottomed flask at 25 °C. Before the exposure to visible light, test solutions with photocatalyst were placed in the dark in order to achieve equilibrium conditions. During the light exposure, for every 20 min, small aliquots were collected, centrifuged at 5000 rpm and the catalyst particles were separated. Thereafter RhB concentration was estimated using UV–Vis spectrophotometer at 554 nm.

The photocatalytic degradation efficiency (η) of RhB was obtained by the following formula

$$\eta = C_0 - C/C_0 \times 100\%$$

where, C is the concentration of the RhB solution at the reaction time t, C_0 is the initial concentration of RhB (at reaction time 0).

Current versus potential (I–V) data of photoelectrochemical (PEC) cells were measured using a LOT-Oriel-Autolab, a 150 W Xenon arc lamp as the light source provided a light power of 100 mW cm^{-2} or 1 sun illumination. Electrochemical impedance spectra (EIS) were measured on an Autolab PGSTAT 302N equiped with a NOVA 1.9 software.

3. Results and Discussion

Figure 1 shows the X-ray diffraction patterns of g-C_3N_4, WO_3 (W), CeO_2 (C), WMCN, and CMCN composites to
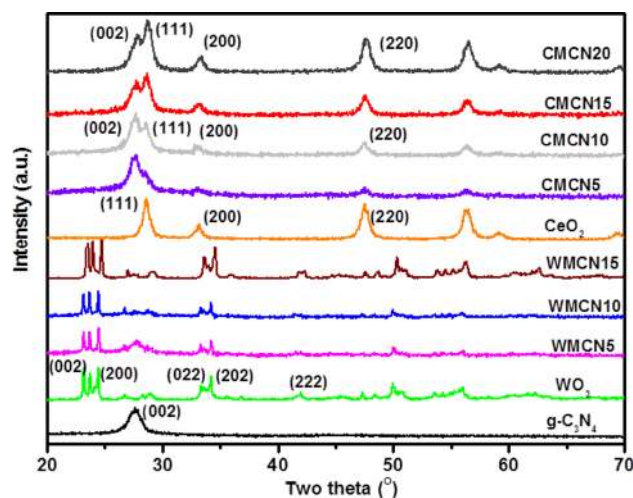
Figure 1. XRD patterns of all the WMCN, CMCN composites along with the g-C_3N_4, WO_3, and CeO_2 materials.

identify the crystal phases of materials. The pronounced peak observed at 27.73° corresponds to (002) plane of the g-C_3N_4 which is attributed to the long-range interlayer stacking of aromatic systems. In WO_3, the peaks were observed at 23.19°, 24.47°, 33.3°, 34.2°, and 41.96° which could be assigned to the monoclinic phase of WO_3 indicated to (002), (200), (022), (202), and (222) plane respectively. The XRD patterns of CeO_2 (ceria) were characterized by peaks at 28.61°, 33.18°, and 47.62° which belong to (111), (200), and (220) planes and confirm the presence of the cubic fluorite structure. From the diffraction patterns of WMCN and CMCN composites, it is observed that the peaks attributed to WO_3, g-C_3N_4, and CeO_2 respectively. This clearly indicates that WO_3 and CeO_2 are successfully introduced on to the g-C_3N_4 material and the g-C_3N_4 peak position slightly changed from 27.73°. It indicates that a small shift of interlayer due to the interaction between metal oxide (WO_3, and CeO_2) and g-C_3N_4.[25]

The BET surface area of the WMCN10, CMCN15, g-C_3N_4, WO_3, and CeO_2 samples was measured by nitrogen adsorption–desorption isotherms and presented in Table 1. The surface area of WMCN10 and CMCN15 is increased by 1.25 and 1.95 times with respect to bare g-C_3N_4. The higher surface area in case of CMCN15 is due to the presence of high surface area CeO_2 material. These composites provide more reaction sites for photodegradation reactions than pure g-C_3N_4.

The FT-IR spectrum of CMCN15, WMCN10, CeO_2, WO_3 and g-C_3N_4 were presented in Figure S1, Supplementary Information. For bare g-C_3N_4, various bands were found in the 798–1650 cm^{-1} region. The peak at 798 cm^{-1} corresponds to the tri *s*-triazine units and the peaks observed at 1639 cm^{-1} attributed to the C=N stretching mode. From 3000 to 3600 cm^{-1} a broad

Table 1. Band gap energy, rate constant (k), and surface area of g-C_3N_4, WO_3, CeO_2, WMCN10, and CMCN15 materials.

Sl. No.	Sample name	Band gap (eV)	Rate constant (min^{-1})	Surface area (m^2/g)
1	g-C_3N_4	2.78	4×10^{-3}	11
2	WO_3 (W)	2.66	4.4×10^{-3}	7
3	CeO_2 (C)	3.01	3×10^{-3}	75
4	WMCN10	2.73	22×10^{-3}	13
5	CMCN15	2.80	10×10^{-3}	22
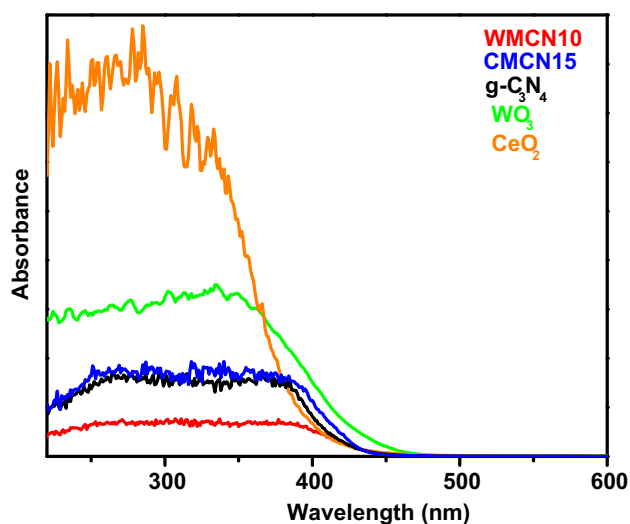
**Figure 2.** UV–Vis spectrum of g-C_3N_4, WO_3, CeO_2, WMCN10, and CMCN15 composites.

absorption band is observed and it is connected to the residual N–H components and the O–H bond from the amino group and absorbed H_2O molecules, respectively. In the case of CMCN15 and WMCN10 also observed similar bands with less intense.[26]

The optical spectrum of the WMCN10 and CMCN15 along with their individuals is shown in Figure 2. The band gap of WO_3, CeO_2, and g-C_3N_4 are 2.78, 3.01 and 2.66 eV respectively, which are calculated from absorption edges. When the WO_3 or CeO_2 were deposited on the g-C_3N_4, the band edge positions were shifted, and

observed band gap for WMCN10 is 2.72 eV, which is shorter than pure g-C_3N_4. It reflects that the light absorption of WMCN10 increases and which improves the photocatalytic performance than other composites.

The WMCN10 and CMCN15 samples were characterized by TGA in the air along with g-C_3N_4 to measure the content of WO_3 in WMCN10 and CeO_2 in CMCN15 materials, and the results were presented in Figure S2, Supplementary Information. In the WMCN10, CMCN15, and g-C_3N_4 materials, around 2–3% of weight loss happened between 303 and 403 K regions, which could be attributed to the presence of adsorbed water. In bare g-C_3N_4, it was found that a rapid weight loss occurred from about 800 to 890 K due to the combustion of g-C_3N_4. Whereas for CMCN15 and WMCN10 composites, it occurred in the temperature range ~740 to 868 K and ~790 to 890 K, which is lower than pure g-C_3N_4. For the CMCN15 and WMCN10 composites up to 740 and 785 K, no considerable weight loss was observed. In the case of CMCN15 after reaching 868 K, the pure g-C_3N_4 was completely burnt; the amounts of CeO_2 in this material can be known from the weight residue after that temperature. Similarly, the amount of WO_3 in WMCN10 can also be calculated. From the TG analysis, the mass contents of WO_3 and CeO_2 in WMC10 and CMCN15 were estimated to be 11.2% and 17.4%, respectively, which is in good accord with the raw material composition.

Figure 3 illustrates the TEM pictures of the g-C_3N_4, WO_3 and WMCN10 materials. As seen in the figure,
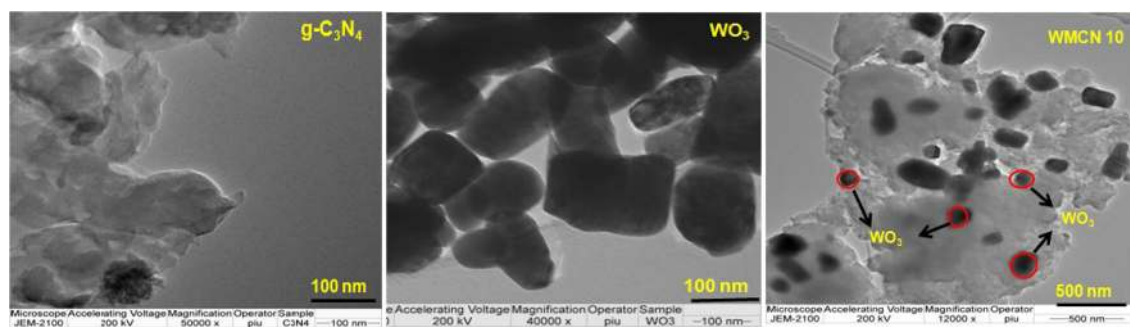
**Figure 3.** TEM images of g-C_3N_4, WO_3 and WMCN10 materials.
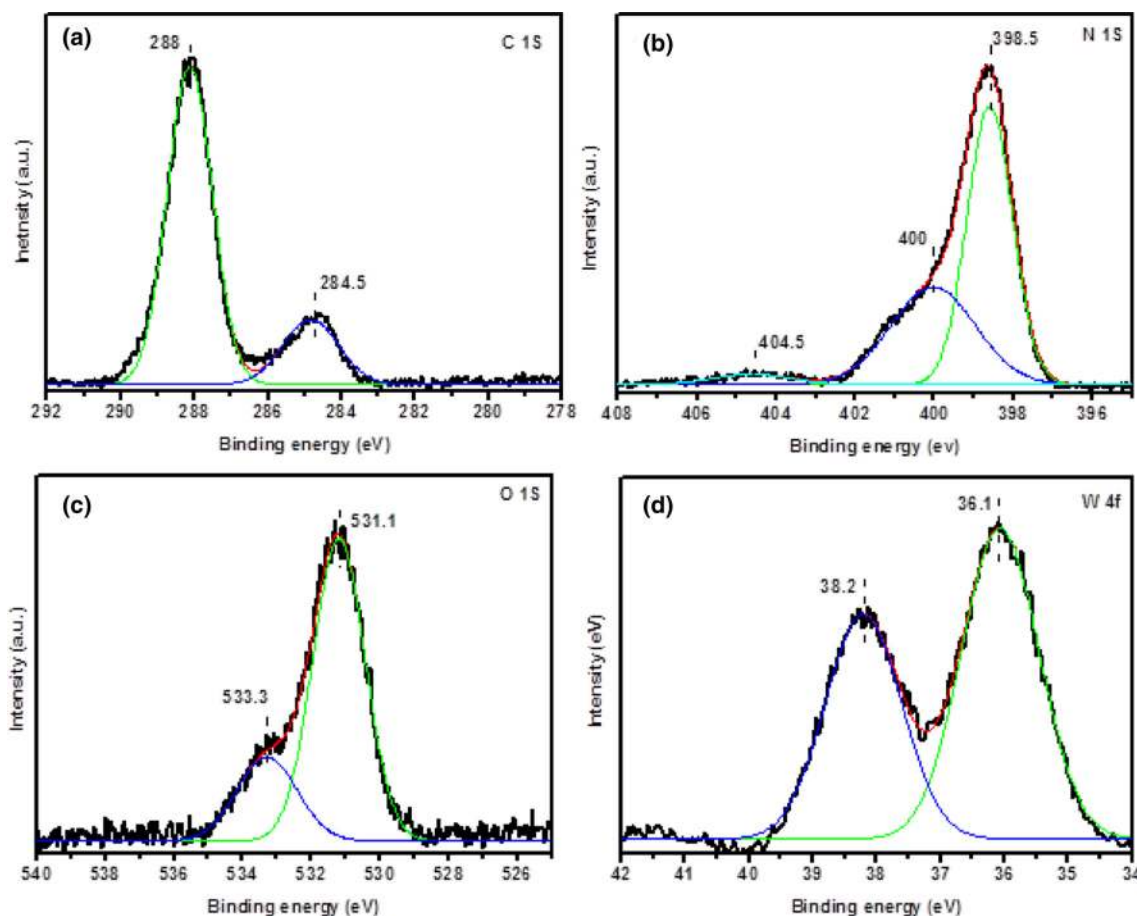
Figure 4.   (a) C 1s, (b) N 1s, (c) O 1s and (d) W 4f XPS of WMCN10 material.

g-C_3N_4 displayed sheet-like structure and WO_3 showed the plate-like shape. In the case of WMCN10, it is clearly visible that WO_3 particles covered over the sheets of g-C_3N_4, which is shown with the red circles and presented in Figure 3. The average particle size of WO_3 measured is around 100–150 nm. Based on the TEM analyses, it can be concluded that the hetero-junction is formed in the composite. To identify the morphology of g-C_3N_4, WO_3, and WMCN10, SEM was used, and images were presented in Figure S3, Supplementary Information.

To explicate the oxidation state of W and kind of elements present in the WMCN10 we characterized the material with XPS and presented in Figure 4. The survey spectrum of WMCN10 material was presented in Figure S4 (Supplementary Information). It reveals that the material is composed of C, N, O and W. These peaks were deconvoluted into Gaussian-Lorentzian shapes and are shown in Figure 4. Figure 4(a) depicts the C 1S spectrum of WMCN10 exhibiting two peaks at 288 and 284.5 eV. The former one corresponds to the carbon atoms bonded with nitrogen atoms in the graphitic structure, and the latter one at 284.5 eV related to the sp^2

C-C bonds from carbon-containing contaminations. In the case of N 1S (Figure 4(b)), three peaks were noticed at 398.5, 400 and 404.5 eV and it is used to know the types of C-N coordination in the material. The first peak assigned to triazine ring (C=N–C) in which nitrogen bonded to two carbon atoms confirming the presence of sp^2-bonded graphitic carbon nitride. The second one at 400 eV is related to quaternary nitrogen atoms bonded to three carbon atoms and the binding energy at 404.5 eV is related to C–N–H. The O 1s (Figure 4(c)) peak observed at 531.1 eV and 533.3 eV. The former one is associated with W–O–H and the second one related to the C=O in g-C_3N_4. In the case of Figure 4(d), the W 4f spectrum shows two peaks at 36.1 and 38.2 eV representing the existence of W in +6 states. However, these values are slightly more than the bare WO_3, and it is attributed to the interaction with the g-C_3N_4 material.[27–29]

From all the characterization techniques it is clear that the WO_3 and CeO_2 successfully deposited on the g-C_3N_4 and these materials exhibited the high surface area and suitable band gap than the g-C_3N_4, which is important for photocatalytic applications.
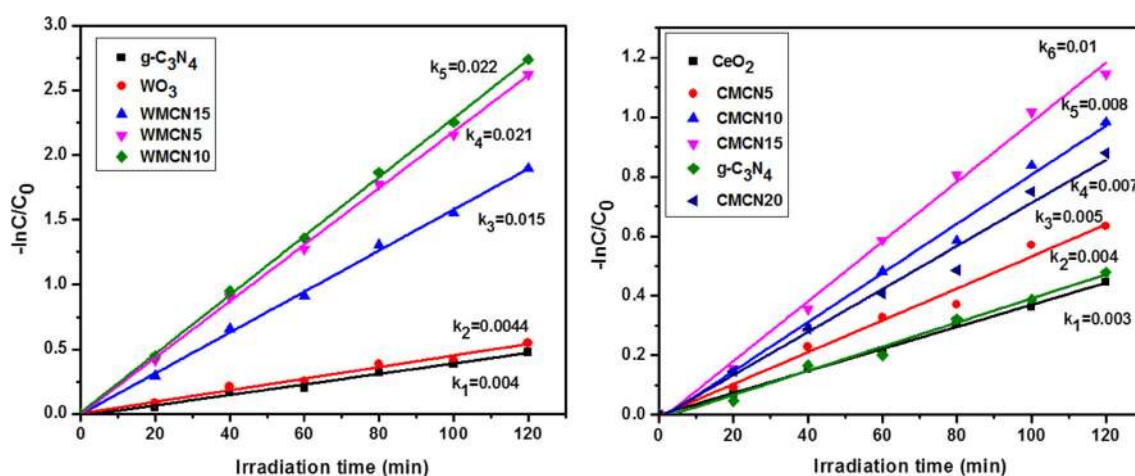
Figure 5. The first order kinetics of WMCN and CMCN materials along with the WO_3, g-C_3N_4, and CeO_2 for RhB degradation (rate constant = k (min^{-1})).

3.1 *Photocatalytic activity*

Rhodamine B (RhB) dye is widely used as a colorant in textiles and food. It causes environmental problems, imbalance non-aesthetic pollution and eutrophication in aquatic life. Hence, the reduction or elimination of this dye pollutant is important.[30,31] Therefore, in the present study, the activity of materials is assessed by the degradation of RhB under visible light.

Initially, we performed the reaction in the absence of a catalyst and in the presence of light and observed no change in the concentration of dye. However, under the dark conditions, in the presence of a catalyst a small change in the concentration is observed due to its adsorption on the catalyst's surface. In the presence of both light and catalyst, the reaction was performed for 2 h, and activity results were presented in Figure S5 (Supplementary Information) and the kinetic plots were given in Figure S6, Supplementary Information. Among the prepared materials, WO_3/g-C_3N_4 and CeO_2/g-C_3N_4 composites exhibited better performance than their counterparts. The photocatalytic activity of WO_3/g-C_3N_4 was tested by varying the contents of WO_3 from 0 to 15 wt% and represented them as WMCN5, WMCN10 and WMCN15. Similarly for the CeO_2/g-C_3N_4 the contents CeO_2 varied from 0 to 20 wt% which are named as CMCN5, CMCN10, CMCN15, and CMCN20. In these, WMCN10 showed excellent performance, nearly 95% of RhB degraded in 120 min and its UV–Vis spectra presented in Figure S7, Supplementary Information. Whereas approximately 68% of the dye was degraded for CMCN15. In both the cases, with an increase of WO_3 and CeO_2 over 10 and 15 wt% the photocatalytic activity of g-C_3N_4 decreased. It may be due to the aggregation of WO_3 or CeO_2 particles on the surface of the g-C_3N_4 material.

The photocatalytic reactions follow the pseudo-first order kinetic equation, which is given below

$$- \ln(C/C_0) = kt \tag{1}$$

where, C_0 and C are the dye concentrations at times 0 and t, respectively, and k is the first-order rate constant.

The first order kinetics of prepared materials for RhB degradation are given in Figure 5. The rate constants (k) of g-C_3N_4, WO_3 and CeO_2 are 0.004, 0.0044 and 0.003 min^{-1} respectively. When WO_3 or CeO_2 present on the g-C_3N_4, the k values are abruptly changed, and it is found more in the case of WO_3/g-C_3N_4 (WMCN) materials. By varying the amount of WO_3 the k values are changed and when the 10 wt% of the WO_3 is present on the g-C_3N_4, it exhibited high photocatalytic performance with k value ~ 0.022 min^{-1} which is 5.5 times more than bare g-C_3N_4. Similar to WMCN materials, CeO_2/g-C_3N_4 materials (5, 10, 15 and 20 wt% of CeO_2) exhibited better photocatalytic performance than g-C_3N_4, and in these, 15wt% CeO_2/g-C_3N_4 (CMCN15) showed higher photocatalytic activity and rate constant (k = 0.008 min^{-1}). In these two kinds of composites WMCN10 and CMCN15, WMCN10 exhibited the better activity with the highest rate constant. This enhanced activity could be attributed to a synergistic interaction between g-C_3N_4 and WO_3, which results, the low recombination rate of charge carriers, high surface area, and increased light absorption.

3.2 *The effect of catalyst amount and dye concentration on the photocatalytic activity*

The WMCN10 composite displayed higher activity among all materials. Therefore, in the current study, we examined the effect of WMCN10 catalyst amount
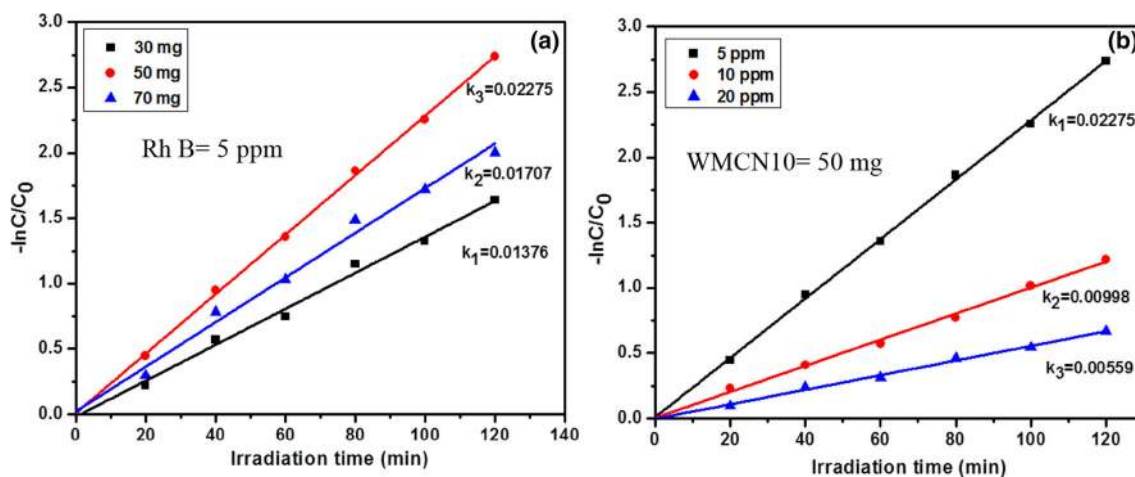
Figure 6. The effect of catalyst amount (a) and dye concentration (b) on the first order kinetics of the RhB degradation (rate constant = k (min^{-1})).

from 30 to 70 mg/L on photocatalytic degradation of dye (Figure S8(a), Supplementary Information). With an increase in the concentration of catalyst from 30 to 50 mg/L, the rate constant increased and from 50 to 70 mg/L, it decreased (Figure 6(a)). Initially, with an increase in the catalyst amount, the number of active sites on the catalyst surface increases, thereby increasing the number of RhB molecules adsorbed on it. However, there is no significant increase in RhB degradation when catalyst concentration reached above 50 mg/L. The excess amount of catalyst acts as a shield, consequently hindering the light penetration, causing the loss of surface area for light harvesting, thus reducing the catalytic activity. Hence, all the experiments were performed with 0.05 g of the catalyst.

By fixing the catalyst amount as 0.05 g, we studied the effect of dye concentration on the photocatalytic activity of WMCN10 (Figure S8(b), Supplementary Information). The dye concentration was changed from 5 to 20 mg/L. The first order kinetic plots were given in Figure 6(b). In general, as the concentration of dye increases, the time for degradation increases. It is due to the decrease in the number of active sites of the catalyst with respect to the number of dye molecules, which prevents the visible light to be absorbed by the catalyst. As a result, the amount of active species formed on the surface of the catalyst decreases, which decreased the activity.[32–34] In the present case, we observed similar results. In every case, the amount of the catalyst (WMCN10), and irradiation time (120 min) were kept constant. All prepared photocatalysts first-order rate constant (k) values are in the following order WMCN10 > WMCN5 > WMCN15 > CMCN15 > CMCN10 > CMCN20 > CMCN5 > WO$_3$ > g-C$_3$N$_4$ > CeO$_2$.

3.3 *Photoelectrochemical (PEC) studies*

The photoelectrochemical performance of as-prepared photoelectrodes such as g-C$_3$N$_4$, WMCN10, and CMCN15 composites was estimated using linear sweep voltammetry (LSV) and results were shown in Figure 7(a). The PEC experiments were employed in a three-electrode system, where the Ag/AgCl and Pt electrodes act as the reference electrode and counter electrodes (CE), respectively. The g-C$_3$N$_4$, WMCN10 and CMCN15 material acts as the working electrode, and 0.1 M Na$_2$SO$_3$ and 0.1 M Na$_2$S mixed solution used as the electrolyte. Upon light illumination, the bare g-C$_3$N$_4$ photoelectrode showed low photocurrent density of 0.045 mA cm^{-2} at 1.23 V vs. reversible hydrogen electrode (RHE). After coating with two different semiconductors like WO$_3$ and CeO$_2$, independently, the photocurrent improved because of heterojunction formation which could reduce the charge recombination. The WMCN10 and CMCN15 composites exhibited the photocurrent density of 1.45 and 0.15 mA cm^{-2} respectively, at 1.23 V vs. RHE. This result clearly shows that the WO$_3$ greatly enhanced g-C$_3$N$_4$ photoelectrochemical performance (PEC) by forming a WO$_3$/g-C$_3$N$_4$ heterojunction. This composite photoelectrode demonstrated the onset photocurrent at 0.21 V vs. RHE. It is worth mentioning that at this potential, other electrodes exhibited negligible current. This low onset potential is due to enhanced charge carrier separation and transportation in the photoanode. Commonly, in PEC cells, the water splitting performance not only depends on the photocurrent density but also on the onset potential, which helps in the charge separation and transportation of photogenerated charge carriers.
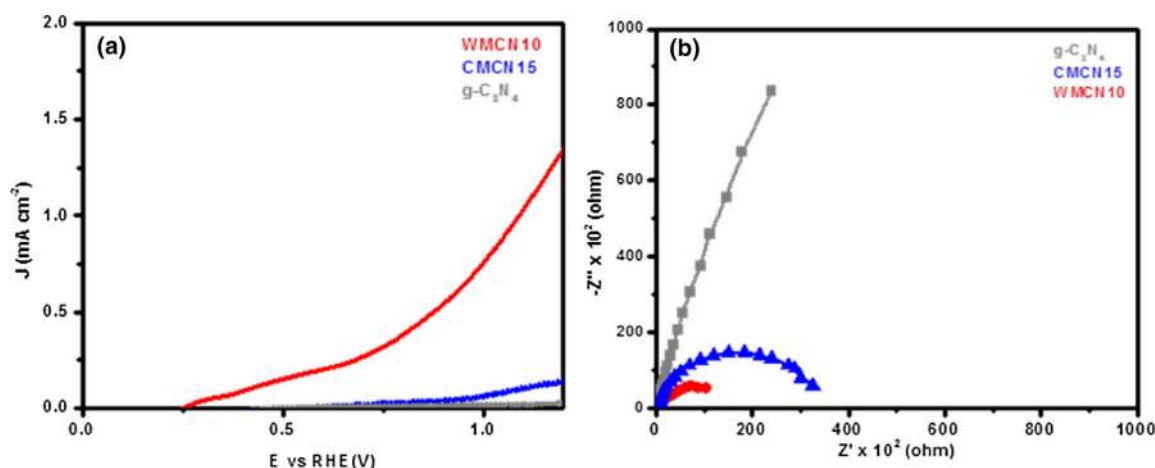
Figure 7. (a) LSV plots of g-C_3N_4, WMCN10, and CMCN15 in 0.1 M Na_2S and Na_2SO_3 electrolyte solution; (b) Electrochemical impedance spectra (EIS) of g-C_3N_4, WMCN10, and CMCN15 composites.

Furthermore, electrochemical impedance spectroscopy (EIS) can explain the interfacial charge transfer resistance (Rct) at the photoanode/electrolyte interfaces. Typically, smaller semicircle obtained from the Nyquist plots suggest the less electron transport resistance, resulting in faster interfacial charge transfer and higher separation of charge carriers. EIS Nyquist plots of the g-C_3N_4, WMCN10, and CMCN15 composites were recorded at a frequency range of 1 MHz to 0.1 Hz under dark conditions, and displayed in Figure 7(b). The EIS plots illustrated that the WMCN10 photoanode exhibited the lowest charge transfer resistance than the bare g-C_3N_4 and CMCN15 composites, and it reflects the higher photocurrent for water splitting. The results reveal that WO_3 plays a vital role in the WO_3/g-C_3N_4 material, which significantly improved the PEC performance of g-C_3N_4.[35]

3.4 *Possible photocatalytic mechanism*

In general, the photoactivity of the material depends on the electron–hole recombination rate, surface area, band gap, etc. From the RhB activity studies, it is clear that the activity of WMCN10 and CMCN15 are better than all other materials. In these two, WMCN10 exhibited more activity. The expected reason for this is the suppression of electron–hole recombination, which is more in WMCN10 material than CMCN15 as can be seen from EIS plots. In addition, generation of electron–hole pairs is more in WMCN10 in which both the semiconductors are visible active, unlike CMCN15 material where CeO_2 is UV active and whose calculated band gap energy is about 3 eV. A keen observation of the electrochemical studies reveals that the electron–hole separation was increased in the WMCN10 material. Therefore, here

we discussed the possible photocatalytic mechanism of WMCN10 for RhB degradation in detail.

To inspect the photocatalytic mechanism of WMCN10, trapping experiments were performed. Three kinds of scavengers IPA (Isopropanol), sodium oxalate, and benzoquinone (BQ) were used to scavenge hydroxyl radicals (•OH), holes (h^+) and superoxide radicals ($O_2^{-•}$) respectively. From Figure S9, Supplementary Information, it is apparent that degradation of RhB decreased by the presence of scavengers compared to without any scavengers. When BQ is added into the reaction medium the photocatalytic activity of WMCN10 was decreased more than the presence of IPA and sodium oxalates, indicating superoxide radicals are the main active species in the RhB degradation followed by holes and hydroxyl radicals.

3.4a *Band gap structures*: The band edge positions of conduction band (CB) and valance band (VB) of a photocatalyst is estimated using the following empirical equation:
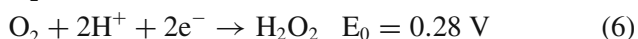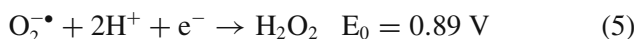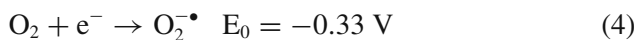
$$E_{vb} = X - E^e + 0.5E_g \qquad (2)$$
$$E_{cb} = E_{vb} - E_g \qquad (3)$$

Where, X is the electronegativity of a semiconductor and its value for WO_3 and g-C_3N_4 are 6.60 and 4.76, respectively. E^e represents the energy of free electrons on the hydrogen scale (about 4.5 eV), E_g corresponds to band gap energy of the semiconductor.[36]

The calculated band gap of WO_3 and g-C_3N_4 from UV–Vis DRS are 2.66 and 2.78 eV. From these, obtained valance band edge potentials of WO_3 and g-C_3N_4 are 3.43 and 1.65 eV and conduction band edge potentials are 0.77 eV and −1.13 eV. Under visible light irradiation, the electrons of WO_3, and g-C_3N_4 were

excited from VB to CB, which left holes in the VB of semiconductors. In photocatalysis, the reactive species were hydrogen peroxide, hydroxyl radicals, superoxide radicals, holes, etc. The electrode potentials required for the formation of these reactive species is given in the following equations.[37] From the scavenger studies, it is confirmed that these are the main active species in degradation of RhB.

$$O_2 + e^- \rightarrow O_2^{-\bullet} \quad E_0 = -0.33 \text{ V} \tag{4}$$

$$O_2^{-\bullet} + 2H^+ + e^- \rightarrow H_2O_2 \quad E_0 = 0.89 \text{ V} \tag{5}$$

$$O_2 + 2H^+ + 2e^- \rightarrow H_2O_2 \quad E_0 = 0.28 \text{ V} \tag{6}$$

$$H_2O + h^+ \rightarrow \bullet OH + H^+ \quad E_0 = 2.32 \text{ V} \tag{7}$$

In case of WMCN10, the conduction band edge potentials of WO_3 is unfavorable to form superoxide radical and hydrogen peroxide due to its high potential, whereas it is possible in the case of g-C_3N_4 since it has low potential. The holes of the WO_3 are favorable to produce hydroxyl radicals because of its high potential, and it is not possible in case of g-C_3N_4, since the valence band edge potential of g-C_3N_4 is unfavourable to form hydroxyl radicals. From the trapping experiments, it is obvious that $\bullet OH$, h^+, and $O_2^{-\bullet}$ are important for degradation of pollutant.

From the above results, the generation of reactive species in WMCN10 is shown schematically in Figure 8. A closer observation of the figure states that the generated electrons in the CB of g-C_3N_4 material reacts with oxygen and form $O_2^{-\bullet}$ species. The conduction band electrons in the WO_3 will transfer to the valence band
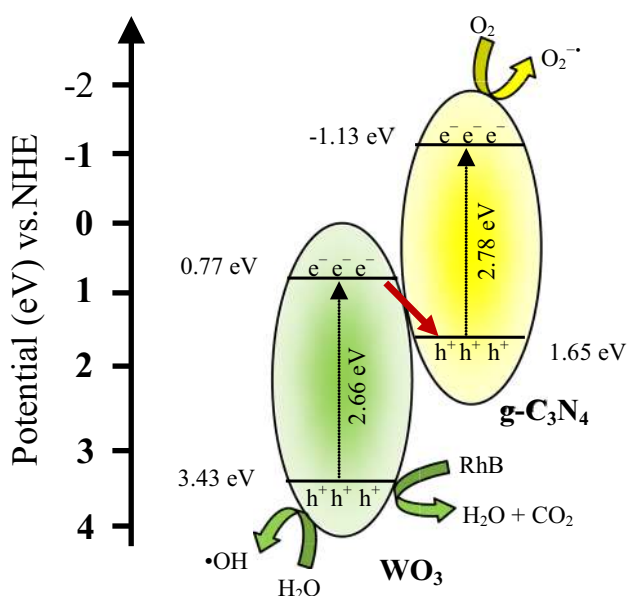
of g-C_3N_4 leaving the holes in the WO_3 material. These holes can directly react with pollutant or form hydroxyl radicals by reacting with the water thereby forming reactive species ($O_2^{-\bullet}$, $\bullet OH$, and h^+), which finally degrade the pollutant.[38]

Finally, the activity of the WMCN10 catalyst towards the RhB degradation is compared with the few literature reported catalysts namely WO_3/Cu,[39] Ce/Mo-V_4O_9,[40] Zn-doped Fe_3O_4,[41] modified carbon nitride,[42] etc. The WMCN10 material was found to be more active than the reported catalysts, which is due to the presence of strong synergistic interaction between g-C_3N_4 and WO_3 compared to all other materials. TOC studies are also performed on the WMCN10 material using Shimadzu TOC analyzer for RhB degradation for 2 h, and 50% mineralization was achieved.

3.5 *Reusability studies*

To assess the recyclability and photostability of WMCN10, recyclability tests are conducted for RhB degradation and presented in Figure S10, Supplementary Information. From the 1st cycle to the 5th cycle, it is apparent that the degradation percentage slightly changed. It means that it remains relatively stable throughout the five runs under visible light irradiation. To know the stability of a catalyst, the spent catalyst was characterized with XRD and presented in Figure S11, Supplementary Information. It represents that the material was structurally stable even after 5 cycles.

4. Conclusions

In summary, a series of WO_3/g-C_3N_4 and CeO_2/g-C_3N_4 composites are successfully synthesized by varying the amounts of WO_3 and CeO_2 and evaluated for the Rhodamine B degradation and photoelectrochemical studies. Among the prepared materials, WMCN10 showed the highest degradation efficiency. 10 wt% of WO_3 on g-C_3N_4 increased the first order rate constant by 5.5 times that of the g-C_3N_4 material. The photocurrent density of WMCN10 photoanode achieved 1.45 mA cm^{-2} at 1.23 V (vs.) RHE and this is much higher than that of bare g-C_3N_4 and CMCN materials. The improved activity of WMCN10 is ascribed to the synergetic interaction between WO_3 and g-C_3N_4, which results in good separation charge carriers and decreased the recombination rate thereby, enhanced its activity. From the scavenger studies, it is concluded that $O_2^{-\bullet}$ species are the major active species in the WMCN10 photocatalytic systems. The present study illustrates that the WO_3/g-C_3N_4 composites can be effectively utilized as a visible light

Figure 8. Schematic illustration of a proposed mechanism for the RhB degradation under visible light.

driven photoactive materials than $CeO_2/g\text{-}C_3N_4$ for a variety of applications.

Supplementary Information (SI)

All additional information pertaining to characterization and activity studies of the materials using FT-IR (Figure S1), TGA (Figure S2), SEM (Figure S3), XP survey spectrum (Figure S4), RhB degradation (%) (Figure S5), RhB degradation (%) with respect to time (Figure S6), Absorption changes of RhB(5ppm) by WMCN10 (Figure S7), Effect of catalyst amount (a) and RhB concentration (b) on RhB degradation (%) (Figure S8 (a) and (b)), Effect of scavengers on the photocatalytic degradation of RhB over WMCN10 material (Figure S9), Cyclic runs of WMCN10 material under visible light irradiation for 2 h (Figure S10) and XRD pattern of fresh and spent WMCN10 material (Figure S11) are given in the supporting information. Supplementary Information is available at www.ias.ac.in/chemsci.

References

1. Wang Z, Huo Y, Fan Y, Wu R, Wu H, Wang F and Xu X 2018 Facile synthesis of carbon-rich g-C_3N_4 by copolymerization of urea and tetracyanoethylene for photocatalytic degradation of Orange II *J. Photochem. Photobiol. A Chem.* **358** 61

2. Li H, Zhao F, Zhang J, Luo L, Xiao X, Huang Y, Ji H and Tong Y 2017 A g-C_3N_4/WO_3 photoanode with exceptional ability for photoelectrochemical water splitting *Mater. Chem. Front.* **1** 338

3. Ashok Kumar K V, Chandana L, Ghosal P and Subrahmanyam C H 2018 Simultaneous photocatalytic degradation of p-cresol and Cr (VI) by metal oxides supported reduced graphene oxide *Mol. Catal.* **451** 87

4. Sun Z, Wang H, Wu Z and Wang L 2018 g-C_3N_4 based composite photocatalysts for photocatalytic CO_2 reduction *Catal. Today* **300** 160

5. Zou W, Shao Y, Pu Y, Luo Y, Sun J, Ma K, Tang C, Gao F and Dong L 2017 Enhanced visible light photocatalytic hydrogen evolution via cubic CeO_2 hybridized g-C_3N_4 composite *Appl. Catal. B Environ.* **218** 51

6. Ye C, Li J X, Li Z J, Li X B, Fan X B, Zhang L P, Chen B, Tung C H and Wu L Z 2015 Enhanced driving force and charge separation efficiency of protonated g-C_3N_4 for photocatalytic O_2 evolution *ACS Catal.* **5** 6973

7. Liu X, Jin A, Jia Y, Xia T, Deng C, Zhu M, Chen C and X Chen 2017 Synergy of adsorption and visible-light photocatalytic degradation of methylene blue by a bifunctional Z-scheme heterojunction of WO_3/g-C_3N_4 *Appl. Surf. Sci.* **405** 359

8. Liang Z Y, Wei J X, Wang X, Yu Y and Xiao F X 2017 Elegant Z-scheme-dictated g-C_3N_4 enwrapped WO_3 superstructures: a multifarious platform for versatile photoredox catalysis *J. Mater. Chem.* A **5** 15601

9. Zhang G, Lan Z A, Lin L, Lin S and X Wang 2016 Overall water splitting by Pt/g-C_3N_4 photocatalysts without using sacrificial agents *Chem. Sci.* **7** 3062

10. Martin D J, Reardon P J T, Moniz S J A and Tang J 2014 Visible Light-Driven pure water pplitting by a Nature-Inspired organic Semiconductor-Based system *J. Am. Chem. Soc.* **136** 12568

11. Yu S, Webster R D, Zhou Y and Yan X 2017 Ultrathin g-C_3N_4 nanosheets with hexagonal CuS nanoplates as a novel composite photocatalyst under solar light irradiation for H_2 production *Catal. Sci. Technol.* **7** 2050

12. Wang C H, Qin D D, Shan D L, Gu J, Yan Y, Chen J, Wang Q H, He C H, Li Y, Quan J J and Lu X Q 2017 Assembly of g-C_3N_4-based type II and Z-scheme heterojunction anodes with improved charge separation for photoelectrojunction water oxidation *Phys. Chem. Chem. Phys.* **19** 4507

13. Dong P, Yang B, Liu C, Xu F, Xi X, Hou G and Shao R 2017 Highly enhanced photocatalytic activity of WO_3 thin films loaded with Pt–Ag bimetallic alloy nanoparticles *RSC Adv.* **7** 947

14. Xiao T, Tang Z, Yang Y, Tang L, Zhou Y and Zou Z 2018 In situ construction of hierarchical WO_3/g-C_3N_4 composite hollow microspheres as a Z-scheme photocatalyst for the degradation of antibiotics *Appl. Catal. B Environ.* **220** 417

15. Vinodkumar T, Naga Durgasri D, Maloth S and Reddy B M 2015 Tuning the structural and catalytic properties of ceria by doping with Zr^{4+}, La^{3+}, and Eu^{3+} cations *J. Chem. Sci.* **127** 1145

16. Jourshabani M, Shariatinia Z and Badiei A 2017 Facile one-pot synthesis of cerium oxide/sulfur-doped graphitic carbon nitride (g-C_3N_4) as efficient nanophotocatalysts under visible light irradiation *J. Colloid Interface Sci.* **507** 59

17. Channei D, Inceesungvorn B, Wetchakun N, Ukritnukun S, Nattestad A, Chen J and Phanichphant S 2014 Photocatalytic degradation of methyl orange by CeO_2 and Fe–doped CeO_2 films under visible light irradiation *Sci. Rep.* **4** 5757

18. Vinodkumar T, Govinda Rao B and Reddy B M 2015 Influence of isovalent and aliovalent dopants on the reactivity of cerium oxide for catalytic applications *Catal. Today* **253** 57

19. Vinodkumar T, Naga Durgasri D, Reddy B M and Alxneit I 2014 Synthesis and structural characterization of Eu_2O_3 doped CeO_2: influence of oxygen defects on CO oxidation *Catal. Lett.* **144** 2033

20. Vinodkumar T, Mukherjee D, Subrahmanyam C H and Reddy B M Investigation on the physicochemical properties of $Ce_{0.8}Eu_{0.1}M_{0.1}O_{2-\delta}$ (M = Zr, Hf, La, and Sm) solid solutions towards soot combustion *New J. Chem.* **42** 5276

21. Li F, Tian X, Yuhong Z, Jun Y, Aiwu W and Zhong W 2015 Preparation of WO_3-reduced graphene oxide

nanocomposites with enhanced photocatalytic property *Ceram. Int*. **41** 5903

22. Chengsi P, Dengsong Z, Liyi S and Jianhui F 2008 Template-Free Synthesis, Controlled Conversion, and CO Oxidation Properties of CeO_2 Nanorods, Nanotubes, Nanowires, and Nanocubes *Eur. J. Inorg. Chem.* **2008** 2429

23. Liying H, Yeping L, Hui X, Yuanguo X, Jixiang X, Wang K, Huaming L and Xiaonong C 2013 Synthesis and characterization of CeO_2/g-C_3N_4 composites with enhanced visible-light photocatalytic activity *RSC Adv*. **3** 22269

24. Liying H, Hui X, Li Y, Huaming L, Xiaonong C, Jixiang X, Yuanguo X and Guobin C 2013 Visible-light-induced WO_3/g-C_3N_4 composites with enhanced photocatalytic activity *Dalton Trans*. **42** 8606

25. Fina F, Callear S K, Carins G M and Irvine J T S 2015 Structural investigation of graphitic carbon nitride via XRD and Neutron Diffraction *Chem. Mater*. **27** 2612

26. Chen Y and Wang X 2018 Template-free synthesis of hollow G-C_3N_4 polymer with vesicle structure for enhanced photocatalytic water splitting *J. Phys. Chem. C* **122** 3786

27. Ansari S A and Cho M H 2017 Simple and large scale construction of MoS_2-g-C_3N_4 heterostructures using mechanochemistry for high performance electrochemical supercapacitor and visible light photocatalytic applications *Sci. Rep.* **7** 43055

28. Yuan X, Duan S, Wu G, Sun L, Cao G, Li D, Xu H, Li Q and D Xia 2018 Enhanced catalytic ozonation performance of highly stabilized mesoporous ZnO doped g-C_3N_4 composite for efficient water decontamination *Appl. Catal. A Gen.* **551** 129

29. Li Y G, Wei X L, Yan X Y, Cai J T, Zhou A N, Yan M R and Liu K Q 2016 Construction of inorganic–organic 2D/2D WO_3/g-C_3N_4 nanosheet arrays toward efficient photoelectrochemical splitting of natural seawater *Phys. Chem. Chem. Phys.* **18** 10255

30. Zhang L, He Y, Wu Y and Wu T 2011 Photocatalytic degradation of RhB over $MgFe_2O_4$/TiO_2 composite materials *Mater. Sci. Eng. B* 176 **1497**

31. Rahman Q I, Ahmad M, Misra S K and Lohani M 2013 Effective photocatalytic degradation of rhodamine B dye by ZnO nanoparticles *Mater. Lett*. **91** 170

32. de Moraes N P, Silva F N, Pinto da Silva M L C, Campos T M B, Thim G P and Rodrigues L A 2018 Methylene blue photodegradation employing hexagonal prismshaped niobium oxide as heterogeneous catalyst: effect of catalyst dosage, dye concentration, and radiation source *Mater. Chem. Phys.* **214** 95

33. Ashok Kumar K V, Amanchi S R, Sreedhar B, Ghosal P and Subrahmanyam C H 2017 Phenol and Cr(VI) degradation with Mn ion doped ZnO under visible light photocatalysis. *RSC Adv*. **7** 43030

34. Karimi-Nazarabada M and Goharshadi E K 2017 Highly efficient photocatalytic and photoelectrocatalytic activity of solar light driven WO_3/g-C_3N_4 nanocomposite *Sol. Energy Mater. Sol. Cells* **160** 484

35. Li J, Hao H and Zhu Z 2016 Construction of g-C_3N_4 − WO_3-Bi_2WO_6 double Z-scheme system with enhanced photoelectrochemical performance *Mater. Lett*. **168** 180

36. Bi C, Cao J, Lina H, Wang Y and Chen S 2016 Enhanced photocatalytic activity of $Bi_{12}O_{17}Cl_2$ through loading Pt quantum dots as a highly efficient electron capturer *Appl. Catal. B Environ*. **195** 132

37. Zhu W, Sun F, Goei R and Zhou Y 2017 Construction of WO_3 − g-C_3N_4 composites as efficient photocatalysts for pharmaceutical degradation under visible light *Catal. Sci. Technol.* **7** 2591

38. Li H, Yu H, Quan X, Chen S and Zhang Y 2016 Uncovering the key role of the Fermi level of the electron mediator in a Z-Scheme photocatalyst by detecting the charge transfer process of WO_3-metal g-C_3N_4 (Metal = Cu, Ag, Au) *ACS Appl. Mater. Interfaces* **8** 2111

39. Ge M, Junlin L, Qingguo M, Haiqin L, Lingling S, Yongguang Z, Mingliang J, Zhihong C, Mingzhe Y, Richard N, Xin W, Chuanyi W, Jun-Ming L and Guofu Z 2018 Synergistic effect of Cu-ion and WO_3 nanofibers on the enhanced photocatalytic degradation of Rhodamine B and aniline solution *Appl. Surf. Sci.* **451** 306

40. Arunadevi R, Kavitha B, Rajarajan M and Suganthi A 2018 Synthesis of Ce/Mo-V_4O_9 nanoparticles with superior visible light photocatalytic activity for Rhodamine-B degradation *J. Environ. Chem. Eng.* **6** 3349

41. Huoshi C and Zhaodong N 2018 Monodisperse Zn-doped Fe_3O_4 formation and photo-Fenton activity for degradation of rhodamine B in water *J. Phys. Chem. Solids* **121** 1

42. Jinpeng Y, Yijun Y, Huimin H, Pengcheng M, Yanhong S and Xia L 2018 Carbon nitrides modified with suitable electron withdrawing groups enhancing the visible-light-driven photocatalytic activity for degradation of the Rhodamine B *Mater. Res. Bull.* **106** 204